Catalysis Today 220–222 (2014) 113–123

Contents lists available at ScienceDirect

Catalysis Today

journal homepage: www.elsevier.com/locate/cattod

Estimation of effective diffusion coefficient and its effect on effectiveness factor for HDS catalytic process: A multi-scale approach

Mario E. Cordero[a,*], Reyna Natividad[b], Luis G. Zárate[a], J.A. Hernandez-Servin[c], Jesús Salas[a]

[a] Escuela de Ingeniería Química, Universidad Popular Autónoma de Puebla, 21 Sur, Barrio de Santiago, C.P. 72410, Puebla, Mexico
[b] Centro Conjunto de Investigación en Química Sustentable UAEM-UNAM, Carretera Toluca-Atlacomulco km 14.5, Toluca Estado de México, Mexico
[c] Fac. de Ing., Cerro de Coatepec, Ciudad Universitaria, C.P. 50100, Toluca, Estado de México, Mexico

ARTICLE INFO

Article history:
Received 1 April 2013
Received in revised form 24 July 2013
Accepted 29 July 2013
Available online 26 September 2013

Keywords:
Hydrodesulphurization HDS
Effective transport coefficients
CFD
Pore structure modeling
Isothermal & non-isothermal effectiveness factors

ABSTRACT

Effectiveness factors have great relevance in multiphase reactors modeling since they are the conventional way of incorporating the effects of intra-particle resistance reaction rate. This work determines the description level effect of catalytic pellet microstructure on mass and energy effective transport coefficients prediction, isothermal and no isothermal. For such a purpose some results about on evaluation of the effective diffusivity and conductivity with the methodology of volume averaging were applied. The obtained results along with a Langmuir–Hinshelwood/Hougen–Watson kinetic expression were applied to establish the concentration and temperature fields in a catalytic particle. The evaluation of concentration field and effectiveness factors were developed using two different models: pseudo-homogeneous mass and energy transport model for a catalytic particle with reaction in all domain, and heterogeneous mass and energy transport model with fluid-catalytic surface interphase reaction for a realistic porous structure model. The results show the differences in concentration and temperature profiles between both models and consequently in effectiveness factors. This could be ascribed to the form of evaluation of effective transport coefficients used in the pseudo-homogeneous model, and presumably to the simple shape of the unit cells used for the solution of the closure problem for the average transport equations with homogeneous reaction.

1. Introduction

The development of modeling techniques for the description of diffusion and reaction in heterogeneous catalysis represents a challenge, mainly due to the limitations of the classical pseudo-homogeneous representations [1–3]. These macroscopic models for diffusion-reaction processes can only implicitly account for the geometrical features of real pore spaces [3–5]. For instance, the standard modeling approach is to consider the catalyst particle as a pseuhomogeneous system where reactants and products can diffuse (molecular or Knudsen diffusion) and react according to a given effective transport coefficient and an intrinsic reaction mechanism. Effective transport coefficients are then required for the evaluation of concentration and temperature fields and transport process that take place in complex porous media. Actually, these coefficients are of paramount importance to characterize the mass and energy transport towards and inside the catalyst. Its experimental determination, however, is still challenging. In addition, such measurements are relatively expensive and time-consuming. It has also been recognized that effectiveness factors exhibit a complex dependence on the pore-level structure of the media [6]. Since the details of the pore-scale flow-pattern in the porous medium cannot be captured due to the macroscopic nature of the experimental approach, numerical and theoretical approximations have been reported with complex pore geometries that resemble more closely the real porous-media structures, i.e. ordered or random packing of different geometric configurations, such as square blocks, spheres, cylinders and parallelepipeds [7–11]. These geometries have been used to reconstruct the pore structure. In addition, Sapoval and co-workers [3] found that one can erroneously estimate the effectiveness factor of a catalyst if the geometrical homogeneities of the active surface are not properly considered. It is worth mentioning that in that study, the analysis of only one pore was considered, for which a complex geometry through fractal structures was built up. A revealing study [12] shows the importance of a realistic representation of the complex structure of the porous medium in the determination of effective transport coefficients. In such a work it was concluded that the porous media whose micro-structure was represented with regular unit

* Corresponding author.
E-mail addresses: marioedgar.cordero@upaep.mx, mecsocg@hotmail.com (M.E. Cordero).

0920-5861/$ – see front matter © 2013 Elsevier B.V. All rights reserved.
http://dx.doi.org/10.1016/j.cattod.2013.07.020

cells does not describe the dispersion in a real porous medium. In studies related to theoretical prediction of effective transport coefficients [8–11] based on the volume averaging methodology, the periodic representation of the micro-structure of the porous medium has been found to be important. This representation of porous structure is motivated by computational limitations, and therefore it is desirable to develop a representation that captures the relevant aspects of the medium, as simple as possible though.

Despite the attempts [12–16] too make use of more realistic representations of the porous medium for the evaluation of transport coefficients, in some way or another it has been appealed to significant simplifications. In this sense, the used periodic unitary cells cannot be so complex because this makes difficult to maintain the periodicity condition and in the case of complex geometric representations of porous media, it has been appealed to the study of small portions for the analysis of transport processes with reaction in porous media, as it is the case of the analysis of a single catalytic pore or a portion of the catalyst represented as a pore network built from fractal structures. Therefore, the evaluation of the effect of more real porous micro-structure in the catalytic particles on effective transport coefficients is a not completed task yet [12]. In this context, there is a rigorous methodology that makes possible, at least in part, the understanding and analysis of phenomena that involve different scales, this is the volume averaging method [17]. By this methodology different systems have been studied, as the diffusion-reaction in a catalytic particle problem [8,9] and the energy and momentum transport in a porous medium problem [9,10]. By using this methodology is possible to develop effective means equations that are valid in the entire domain from equations that are only valid in each of the individual phases. The existing literature regarding volume averaging methodology usually deals only with the deduction and presentation of the equations of transport of effective medium along with the conditions under which they are applicable. More recently, volume averaging methodology has aided to establish adequate boundary conditions for transport equations [18]. It is not difficult neither to find the effective transport coefficients evaluation by means of such a methodology. In this context, what is scarce, however, is the application of these developments [19]. In this work, we intend to use the information of the effect of the porous micro-structure through the effective coefficients of transport on the effectiveness factors for catalytic pellets in which a hydrodesulphurization (HDS) reaction of light gasoil takes place. Evidently, the effectiveness factors have great relevance on the HDS reactors modeling and their value strongly influences the behavior of the reactor since they are the conventional form of incorporating the effects of intra-particle resistances to the reaction rate. For the case of Langmuir–Hinshelwood/Hougen–Watson's kinetic rate expressions (LHHW) of a HDS process, the effectiveness factors dependence is usually described in terms of the denominated corrected Module of Thiele [20]. The interest of accurate prediction of catalyst effectiveness factor of the gas oil hydrodesulphurization process has been previously reported [21]. This has been mainly pursued by approximate analytical methods [22,23], by establishing more accurate kinetic models of the HDS reaction, as LHHW [24,25] models, and by taking into account the geometry effect on effectiveness factors [26]. Regarding the effect of the micro-structure on effectiveness factors, network pores built from fractals structures have been employed [14,15,27,28]. The kinetics used in most of these studies has been rather simplistic (power law model) though and a realistic porous structure to determine the effective transport coefficients has not been employed. Thus, this work aims to evaluate the isothermal and no isothermal effectiveness factors for a spherical catalytic particle by means of a heterogeneous mass and energy model with reaction at the solid–fluid interphase at pore scale and pseudo homogeneous mass and energy model with reaction at all catalyst pellet using a realistic microstructure.

Table 1
Kinetic experimental parameters for an HDS process.

$k = k_0 e^{(-(E/RT))}$ [Pa h]$^{-1}$	$k_A^0 = 5.66 \times 10^3$ ppm^{-1}
$k_0 = 0.53$ [Pa h]$^{-1}$	$Q_A = -60.96$ J/mol
$E = 65.95 \times 10^{-3}$ J/mol	$k_H^0 = 1.01 \times^8$ Pa^{-1}
$k_A = k_A^0 e^{(Q_A/RT)}$ ppm^{-1}	$Q_H = -179.76$ J/mol
$k_H = k_H^0 e^{(Q_H/RT)} = 2.004 \times 10^{-8}$ Pa^{-1}	

2. Theory

2.1. Kinetic model

In this work, we evaluate an effectiveness factor that involves a HDS process for light Gasoil following a previously reported LHHW kinetics [29],

$$\langle r_A \rangle^\gamma = \frac{k \langle C_{A_\gamma} \rangle^\gamma \langle p_{H_\gamma} \rangle^\gamma}{(1 + k_A \langle C_{A_\gamma} \rangle^\gamma)(1 + k_H \langle p_{H_\gamma} \rangle^\gamma)} \tag{1}$$

This kinetic model considers that both the sulfurated species and the hydrogen chemisorb on different active sites. The Table 1 shows the used parameters [29]. In the previous expression $\langle r_A \rangle^\gamma$ is reaction rate, $\langle C_{A_\gamma} \rangle^\gamma$ is sulphureted species concentration, $\langle p_{H_\gamma} \rangle^\gamma$ is partial pressure of hydrogen, k, k_A and k_H are the rate and the adsorption constants for sulfurated species and hydrogen, respectively.

In Table 1, k_0, k_A^0 and k_H^0 are the pre-exponential factor for reaction constant and pre-exponential factor for adsorption constant for sulfurated species and the hydrogen respectively; E, Q_A and Q_H are the activation energy and the characteristic energy of the adsorption constant for sulfurated species and the hydrogen, respectively

In Table 2, $\langle \omega_{A_\gamma} \rangle^\gamma$, X, Y and $\langle \Phi \rangle$ are the dimensionless concentration, dimensionless characteristics lengths and the Thiele modulus for pseudo-homogeneous model; while, ω_{A_γ} and Φ are the dimensionless concentration and the Thiele modulus for the heterogeneous model.

The concentration and temperature fields are obtained from the solution of 2D mass and energy transport equations, by means of two different models, (a) the mass and energy with reaction in the whole domain (pseudo-homogeneous model), (b) the mass and energy transport heterogeneous model with reaction in the interface fluid-catalyst ($\gamma - \kappa$).

2.2. Pseudo-homogeneous transport model

The mass and energy transport equations at spherical catalytic particle scale are [30],

$$\left(\frac{\partial}{\partial x} \mathbf{e}_x + \frac{\partial}{\partial y} \mathbf{e}_y \right) \cdot \left[\varepsilon_\gamma D_{eff} \cdot \left(\frac{\partial \langle C_{A_\gamma} \rangle^\gamma}{\partial x} \mathbf{e}_x + \frac{\partial \langle C_{A_\gamma} \rangle^\gamma}{\partial y} \mathbf{e}_y \right) \right] = \langle r_A \rangle \tag{2}$$

Table 2
Dimensionless parameters and variables.

$\langle \omega_{A_\gamma} \rangle^\gamma = \frac{\langle C_{A_\gamma} \rangle^\gamma}{\langle C_{A_\gamma}^S \rangle^\gamma}$	$\omega_{A_\gamma} = \frac{C_{A_\gamma}}{\langle C_{A_\gamma}^S \rangle^\gamma}$
$\langle \Phi \rangle = \sqrt{\frac{R_p^2 k_1}{\varepsilon_\gamma D_{eff}}}$	$\phi = \frac{1}{k_A \langle C_{A_\gamma}^S \rangle^\gamma}$
$\langle \phi \rangle = \left(\langle C_{A_\gamma}^S \rangle^\gamma \right)^{-1}$	$X = \frac{x}{R_p}$
$\Phi = \sqrt{\frac{k_2 R_p}{D_\gamma}}$	$Y = \frac{y}{R_p}$

$$\left(\frac{\partial}{\partial x}\mathbf{e}_x+\frac{\partial}{\partial y}\mathbf{e}_y\right)\left[K_{eff}\cdot\left(\frac{\partial\langle T\rangle}{\partial x}\mathbf{e}_x+\frac{\partial\langle T\rangle}{\partial y}\mathbf{e}_y\right)\right]=-(\Delta H)\langle r_A\rangle \tag{3}$$

where Eqs. (2) and (3) are for arbitrary domain. The boundary conditions are given by the following equations,

$$\begin{aligned}\frac{\partial\langle C_{A_\gamma}\rangle^\gamma}{\partial x}\mathbf{e}_x+\frac{\partial\langle C_{A_\gamma}\rangle^\gamma}{\partial y}\mathbf{e}_y&=0,\\ \frac{\partial\langle T\rangle}{\partial x}\mathbf{e}_x+\frac{\partial\langle T\rangle}{\partial y}\mathbf{e}_y&=0\quad\text{at}\quad r=0.\end{aligned} \tag{4}$$

$$\langle C_{A_\gamma}\rangle^\gamma=C^s_{A_\gamma},\ \langle T\rangle=\langle T\rangle^s\ \text{at}\quad r=R_p \tag{5}$$

where R_p is the radius of the spherical catalytic particle. Here D_{eff} and K_{eff} are the effective diffusivity and thermal conductivity, ε_γ is the porosity, $-\Delta H$ is the reaction heat, $\langle T\rangle$ is the variable temperature, $C^s_{A_\gamma}$ and $\langle T\rangle^s$ are the temperature and concentration at catalytic surface condition.

2.3. Heterogeneous transport model

In this model, at pore scale, the catalytic pellet is assumed to be constituted by liquid γ and solid κ phases, and the reaction takes place on the fluid–solid interphase $\gamma-\kappa$. The mass transport is given by [17],

$$D_\gamma\left(\frac{\partial^2 C_{A_\gamma}}{\partial x^2}+\frac{\partial^2 C_{A_\gamma}}{\partial y^2}\right)=0\qquad\gamma-\text{phase} \tag{6}$$

The heterogeneous energy transport equation with reaction on the catalytic surface $A_{\gamma\sigma}$ at pore scale is

$$\begin{aligned}k_\gamma\left(\frac{\partial^2 T_\gamma}{\partial x^2}+\frac{\partial^2 T_\gamma}{\partial y^2}\right)&=0\qquad\gamma-\text{phase};\\ k_\sigma\left(\frac{\partial^2 T_\sigma}{\partial x^2}+\frac{\partial^2 T_\sigma}{\partial y^2}\right)&=0\qquad\sigma-\text{phase}.\end{aligned} \tag{7}$$

The Eqs. (6) and (7) are subjected to the pertinent boundary conditions at $A_{\gamma\sigma}$:

$$\begin{aligned}-\mathbf{n}_{\gamma\sigma}\cdot D_\gamma\left(\frac{\partial^2 C_{A_\gamma}}{\partial x^2}\mathbf{e}_x+\frac{\partial^2 C_{A_\gamma}}{\partial y^2}\mathbf{e}_y\right)&=r_A,\\ -\mathbf{n}_{\gamma\sigma}\cdot k_\gamma\left(\frac{\partial^2 T_\gamma}{\partial x^2}\mathbf{e}_x+\frac{\partial^2 T_\gamma}{\partial y^2}\mathbf{e}_y\right)&=(-\Delta H)r_A,\\ \mathbf{n}_{\gamma\sigma}\cdot k_\gamma\left(\frac{\partial^2 T_\gamma}{\partial x^2}\mathbf{e}_x+\frac{\partial^2 T_\gamma}{\partial y^2}\mathbf{e}_y\right)&=-\mathbf{n}_{\gamma\sigma}\cdot k_\sigma\left(\frac{\partial^2 T_\sigma}{\partial x^2}\mathbf{e}_x+\frac{\partial^2 T_\sigma}{\partial y^2}\mathbf{e}_y\right),\\ T_\gamma&=T_\sigma,\end{aligned} \tag{8}$$

and also we have at $A_{\gamma\sigma}$:

$$C_{A_\gamma}=C^s_{A_\gamma} \tag{9}$$

$$T_\sigma=T_\gamma \tag{10}$$

Here D_γ is the bulk diffusivity of the sulfurous species in the mixture, k_γ and k_σ are the fluid γ and solid σ thermal conductivities, C_{A_γ} is the local sulphureted species concentration, T_γ and T_σ are the local temperatures for the solid and fluid phases respectively, $\mathbf{n}_{\gamma\sigma}$ is the normal unitary vector pointing from γ-phase toward the σ-phase, r_A is the surface reaction rate, and $A_{\xi e}$ is the entrance area to the phase ξ.

The kinetic expression of the pseudo-homogeneous model is related to the interfacial kinetics of heterogeneous model at pore scale by means of the following expression [17],

$$\langle r_A\rangle^\gamma=a_v r_A \tag{11}$$

where $a_v=A_{\gamma\kappa}/V$ is the ratio of the fluid-catalyst interfacial area to volume average [17]. The kinetics was adapted from that obtained in a pseudo-homogenous media [29]. This is coherent with the model of reaction at the interface.

2.4. Realistic geometrical model of the porous structure

At pore scale, the vectored model of a real porous media Fig. 1 was built up from a micrograph found in literature [31]. This was adapted in order to replicate parameters comparable to typical values of HDS systems such as pore diameter d_p =20–200 nm [32,33] and porosity $0.3\le\varepsilon_\gamma\le0.6$ [34]. According to this, a more realistic

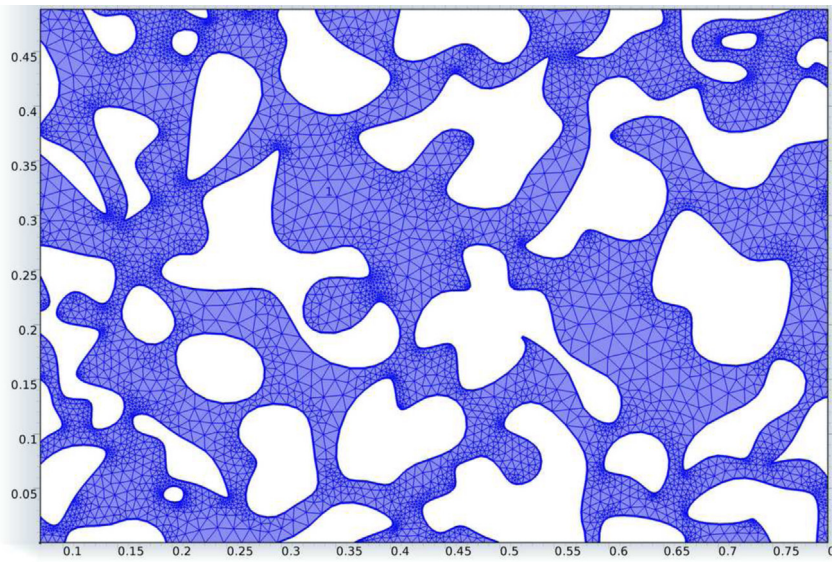

Fig. 1. Vectored micrograph of a model of pore distribution.

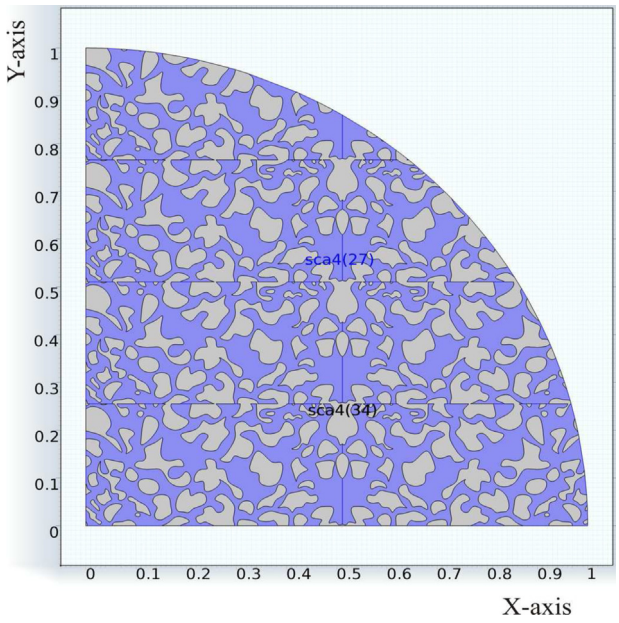

Fig. 2. View of $\frac{1}{4}$ catalytic pellet showing both phases, built from realistic model of pores medium at scale 4:1.

geometrical model than the one based on cubic cells was built for a catalytic particle of 1 mm of diameter, at scales of 4:1 and 2:1 of the real scale Fig. 2.

2.5. Evaluation of the transport effective coefficients

The pseudo-homogeneous model, Eqs. (2)–(5), requires the accurate evaluation of the effective diffusion and effective conductivity coefficients. The theoretical way to evaluate these coefficients through the method of volume averaging can be found in literature [17]. Such studies already suggest the dependence of such parameters with the porous structure and is accepted that a simplified representation of the porous media is enough to capture necessary information of the porous structure and how it can be transported to another length-scale. Fig. 3 depicts the type of periodic representative unitary cells (RUC) used to represent the complex porous media.

Expressions that allow us to evaluate the transport effective coefficients, which is a boundary value problem for the closure vector $\mathbf{b}_\gamma$, are a result of the averaging process of valid punctual transport equations in individual phases, of decomposition of scales [35] of the local transport equations Eq. (15) and a proposal of a solution to the problem for the deviations field C_{A_γ}, expressed in terms of the source that appears in the boundary value problem for the deviations. Eqs. (12) and (13) show the superficial averaging operator and the intrinsic average operator, respectively, used for spatial smoothing of the transport equations previously mentioned. The Eq. (14) shows the relationship between the average surface operator and the operator intrinsic average. The Eq. (15) represents the aforementioned decomposition of scales [35].

$$\langle \Psi_\gamma \rangle^\gamma |_{\mathbf{x}} = \frac{1}{V} \int_{V_\gamma(\mathbf{x})} \Psi_\gamma \left|_{\mathbf{x}+\mathbf{y}_\gamma} \right. dV \tag{12}$$

$$\langle \Psi_\gamma \rangle^\gamma |_{\mathbf{x}} = \frac{1}{V_\gamma(\mathbf{x})} \int_{V_\gamma(\mathbf{x})} \Psi_\gamma \left|_{\mathbf{x}+\mathbf{y}_\gamma} \right. dV \tag{13}$$

$$\langle \Psi_\gamma \rangle |_{\mathbf{x}} = \varepsilon_\gamma \langle \Psi_\gamma \rangle^\gamma |_{\mathbf{x}} \tag{14}$$

$$\Psi_\gamma = \Psi_\gamma + \langle \Psi_\gamma \rangle^\gamma \tag{15}$$

In the previous expressions, the variable $\mathbf{x}$ represents the position vector that locates the centroid of the average volume V, $\mathbf{y}_\gamma$ is a vector relative to the vector $\mathbf{x}$ used to locate any points inside the average volume and V_γ is the volume occupied by the fluid phase. From Eqs. (12) or (13) is clear that the right side term inside the integral depends on $\mathbf{x}+\mathbf{y}$, while the left side quantity only depends on $\mathbf{x}$, that is, the application of the average operator produces a spatial smoothing [17]. The expressions that allow us to evaluate the effective diffusivity D_{eff} and effective thermal conductivity are K_{eff} [17],

$$D_{eff} = D_\gamma \left(\mathbf{I} + \frac{1}{V_\gamma} \int_{A_{\gamma\sigma}} \mathbf{n}_{\gamma\sigma} \mathbf{b}_\gamma dA \right) \tag{16}$$

$$\frac{K_{eff}}{k_\gamma} = (\varepsilon_\gamma + \varepsilon_\sigma \kappa)\mathbf{I} + \frac{(1-\kappa)}{V} \int_{A_{\gamma\sigma}} \mathbf{n}_{\gamma\sigma} \mathbf{b}_\beta dA \tag{17}$$

where $\kappa = k_\sigma / k_\gamma$ is the quotient of conductivity of solid phase to fluid pahse, $\mathbf{I}$ is the identity tensor and ε_σ is the fractions volume of the solid phase. The transport coefficients required by the mass and energy effective medium balances, are obtained from the respective closure problem, which are shown below.

2.5.1. Boundary value problem for closure vector $\boldsymbol{b}_\xi$

The boundary value problem for the closure of the mass averaged transport equations with reaction at all domains [17] is as follows:

$$\nabla^2 \mathbf{b}_\gamma = 0 \tag{18}$$

with the following boundary conditions:

$$-\mathbf{n}_{\gamma\sigma} \cdot \nabla \mathbf{b}_\gamma = \mathbf{n}_{\gamma\sigma} \quad \text{at} \quad A_{\gamma\sigma} \tag{19}$$

$$\mathbf{b}_\gamma(\mathbf{r} + l_i) = \mathbf{b}_\gamma(\mathbf{r}) \quad \text{for} \quad i = 1, 2, 3, \ldots \tag{20}$$

The boundary value problem for the closure of the energy averaged transport equations with generation of energy by reaction at all domains is:

$$\nabla^2 \mathbf{b}_\beta = 0, \qquad \nabla^2 \mathbf{b}_\sigma = 0 \tag{21}$$

with the following boundary conditions:

$$\begin{aligned} \mathbf{b}_\beta &= \mathbf{b}_\sigma; \\ -\mathbf{n}_{\gamma\sigma} \cdot \nabla \mathbf{b}_\beta &= -\mathbf{n}_{\beta\sigma} \cdot \kappa \nabla \mathbf{b}_\sigma + \mathbf{n}_{\beta\sigma}(1-\kappa) \quad \text{at} \quad A_{\gamma\sigma} \end{aligned} \tag{22}$$

$$\begin{aligned} \mathbf{b}_\beta(\mathbf{r} + l_i) &= \mathbf{b}_\beta(\mathbf{r}); \\ \mathbf{b}_\sigma(\mathbf{r} + l_i) &= \mathbf{b}_\sigma(\mathbf{r}) \end{aligned} \tag{23}$$

for $i = 1, 2, 3, \ldots$

Here $\mathbf{b}_\gamma$ and b_β are the closure vectors corresponding to the fluid phase and is convenient to distinguish them because the first one corresponds to the solution of the Eqs. (18)–(20), while the second one corresponds to the solution of the Eqs. (21)–(23). The $\mathbf{b}_\sigma$ vector is the closure vector for solid phase. Also, $\mathbf{n}_{\gamma\sigma} = \mathbf{n}_{\beta\sigma}$ is the normal unitary vector to the fluid–solid interface, r is the position vector that locates any points in the average volume, and l_i represent the three non-unique lattice vectors that are required to describe a spatially periodic porous medium [36].

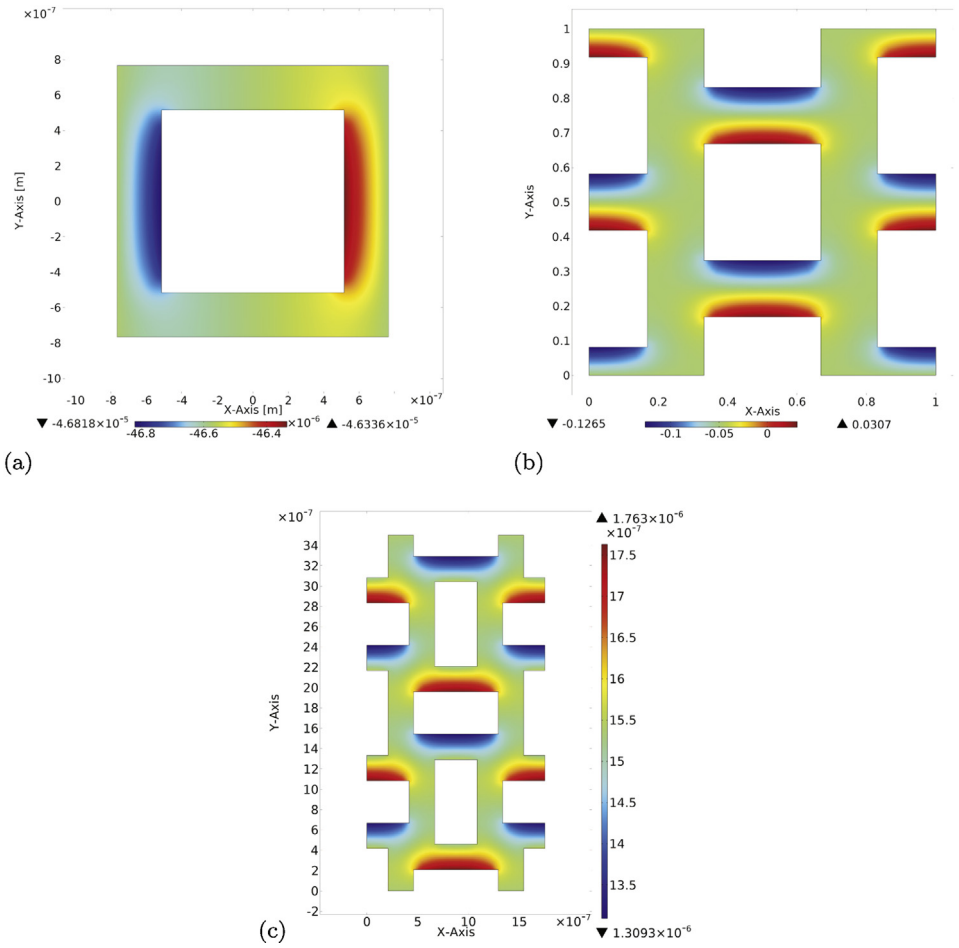

Fig. 3. (a) The x-component of the vector field $\mathbf{b}_\gamma$ in a centered square RUC CC. (b) The x-component of the vector field $\mathbf{b}_\gamma$ in a square alternate RUC CA. (c) The x-component of the vector field $\mathbf{b}_\gamma$ in a rectangular alternate RUC RA.

2.6. Effectiveness factor

The effectiveness factor can be evaluated by the following expression [30],

$$\eta = \frac{1}{W_C r'_{A|S}} \int r'_A dW_C \tag{24}$$

In related effectiveness factors studies, an analysis by means of dimensionless parameters and numbers is usually carried out in order to evaluate the effectiveness factors and is a common practice to dimensionless the transport equations. The η variable is the effectiveness factor, W_C is the catalyst weight and r'_A is the reaction rate in mol(kg cat s^{-1}).

Table 2 shows the dimensionless variables and parameters definition used in this work. It is important to mention that in the dimensionless process of the transport equations at both scales, the Thiele modulus was pursued to be independent of temperature $\langle\Phi_{iso}\rangle$ and in the same way consistency was also pursued in the non-isothermal effectiveness factor evaluation with the isothermal case.

Table 3 shows physical parameters fed to solve the model, whereas Table 2 shows the used dimensionless parameters. In particular, Table 4 shows the relationship between the Thiele modulus $\langle\Phi\rangle$ and the Thiele modulus Φ_{iso} independent from the temperature for the case of the pseudo-homogeneous transport as for Table 5 the same relationship Φ and Φ_{iso} is shown, but for the heterogeneous transport; while β and $\langle\beta\rangle$ are the Prater number defined for

Table 3
Transport and physical parameters used in models.

$\langle P_H^\gamma\rangle^\gamma = 7580.0$ kPa	$\varepsilon_\gamma = \frac{V_\gamma}{V_\gamma+V_\sigma} = 0.5465$
$\langle C_A^\gamma\rangle^\gamma = 84.41$ mol m^{-3}	$a_v = \frac{A_{\gamma\sigma}}{V_\gamma+V_\sigma} = 23191.6$ m^{-1}
$\langle -\Delta H\rangle = -4, 33, 436$ J/mol	$D_{eff} = 1.4629 \times 10^{-5}$ m^2 s^{-1}
$\langle T\rangle^S = 598$ K	$D_\gamma = 3.3817 \times 10^{-5}$ m^2 s^{-1}
$k_\gamma = 4.2 \times 10^{-4}$ cal/(s cm °C)	$K_{eff} = 2.61 \times 10^{-3}$ cal/(s cm °C)
$k_\sigma = 0.508$ cal/(s cm °C)	

Table 4
Relationship between Thiele modulus $\langle\Phi\rangle$ and Isothermal Thiele modulus $\langle\Phi_{iso}\rangle$ for the pseudo-homogenous model.

$\langle\Phi_{iso}\rangle^2 = \left(\frac{k_{T_{iso}} R^2}{\varepsilon D_{eff}}\right)$	$\langle\Phi_{iso}\rangle^2 = \frac{\langle\Phi\rangle^2}{\phi_1+1}$
$k_{T_{iso}} = k_T(\phi_1+1)^{-1}$	$k_T = k_s^0\phi_0\phi_1$
$\phi_0 = \left(C_{A_b} k_{A_S}\right)^{-1}$	$\phi_1 = \left(\langle P_H^\gamma\rangle^\gamma k_{H_s}\right)^{-1}$
$k_s^0 = k_0 e^{-\gamma_E}\langle P_H^\gamma\rangle^\gamma = k^0 e^{-\gamma_E}$	

Table 5
Relationship between Thiele modulus Φ and Isothermal Thiele modulus Φ_{iso} for pseudo-homogenous model, and β parameter in both pseudo-homogenous and heterogeneous models.

$\Phi_{iso}^2 = \frac{Rk_{T_{iso}}}{a_v D_\gamma}$	$\langle\Phi_{iso}\rangle^2 = \Phi^2\left(\frac{Ra_v D_\gamma}{\varepsilon_\gamma D_{eff}}\right)$
$\beta = \left(\frac{-\Delta H \cdot D_\gamma \langle C_A^\gamma\rangle^\gamma\rangle_S}{k_\gamma \langle T_\gamma\rangle^\gamma\rangle_S}\right)$	$\langle\beta\rangle = \frac{k_\gamma D_{eff}}{K_{eff} D_\gamma}\beta$

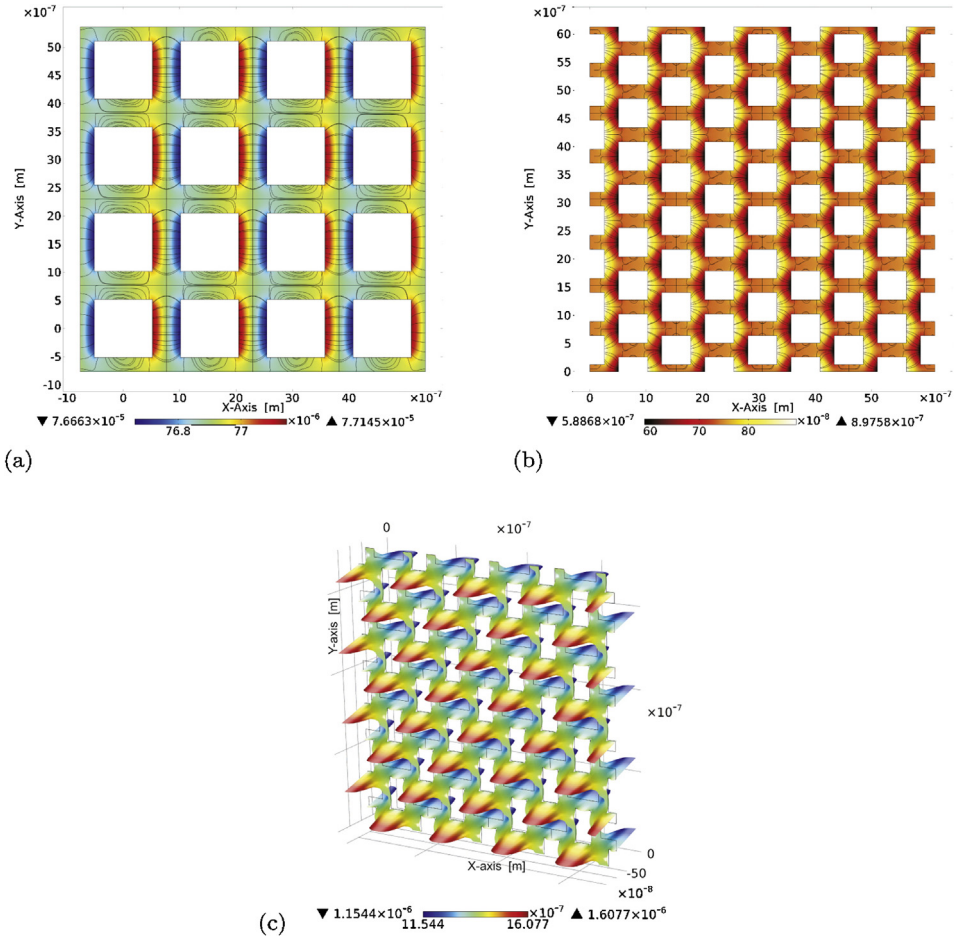

Fig. 4. (a) The *x*-component of the vector field $\mathbf{b}_\gamma$ in a 4×4 coupling of RUC CC. (b) The *x*-component of the vector field $\mathbf{b}_\gamma$ in a 4 × 4 coupling of dimensionless RUC CA. (c) The *x*-component of the vector field $\mathbf{b}_\gamma$ in a 4×2 coupling of RUC RA.

both, heterogeneous and pseudo-homogeneous models; Also V_σ is the solid phase volume, and $k_{T_{iso}}$ and k_T are both, isothermal and no-isothermal dimensionless constant rates, repectively.

3. Results and discussion

For the realistic model construction of the porous structure a pore size distribution previously reported [32,33] of $CoMo/\gamma - Al_2O_3$ was taken into account. According to this reference, 65% of the pores are in a range of d_p =20–200 nm, and 5% d_p> 200 nm [33]. Due to computing resources limitations a pellet diameter of $d_p = 2.5 \times 10^{-7}$ m was chosen. The vectored model adjustment [31] to pore diameter values with the order of $d_p \approx 2.5 \times 10^{-7}$ m, leads to $\varepsilon_\gamma = 0.5465$. The superficial area of a spherical catalyst with radius R=0.5 mm built from the vectored model at scale 2:1 is $A_{\gamma\sigma}$ =458.348 m^2 and at the scale of 4:1 is $A_{\gamma\sigma}$ =88.975 m^2.

It is worth noticing that the built porous structure proposed in this study incorporates geometrical complexity of the porous medium through the minimum characteristics established in previous theoretical models based on the volume averaging methodology [7,17,37–39]. Albeit considering some characteristics (i.e. porosity and pore diameter) of a HDS catalyst, the effect of the spatial porous structure was not captured in the model yet. This may imply some degree of uncertainty that at this stage cannot be ruled out. Therefore is advisable to deepen in the study of this variable so that the importance of its effect can be established in order to decide whether or not to include it in future models. Different RUC's were built Fig. 3, and these were adjusted in such a way that $d_p = 2.5 \times 10^{-7} m$ and $\varepsilon_\gamma = 0.5465$. With these RUC's different couplings were arranged with them Fig. 4, the whole porous structure of a pellet with radius R=0.5 mm Fig. 5 was built up.

The evaluation of the boundary values for vector $\mathbf{b}_\gamma$, Eqs. (18)–(20), in the different RUC's depicted in Fig. 3 was carried out with the help of the commercial software COMSOL Multiphysics, while the same equations evaluation on the various couplings of the RUC's is shown in Fig. 4.

The same evaluation in pellets reconstructed with RUC's and with our realistic model of the porous structure is shown in Fig. 5. With closure vector field $\mathbf{b}_\gamma$ evaluation, we evaluate the effective diffusivity coefficients according to equation Table 6 shows the estimated values of the effective diffusion coefficient through all the mentioned schemes.

The RUC CC was taken as reference and the deviations of the of values of D_{eff} were evaluated by the other schemes. The difference between the RUC CC and the RUC CA is 7.2% for the *x* component and 1.2% for the *y* component, while between the RUC CC and the RUC RA the difference is 10% for the *x* component and 9.7% for the *y* component. It can be observed that the variation of the coupled RUC’ s is not significant, with a slight variation between RUC CA and their couplings of only 2%. This is in concordance with literature where has been stated that is not necessary to build up the whole porous medium with couplings RUC’ s since one periodic RUC gives results equivalent to those obtained by several couples [9–11].

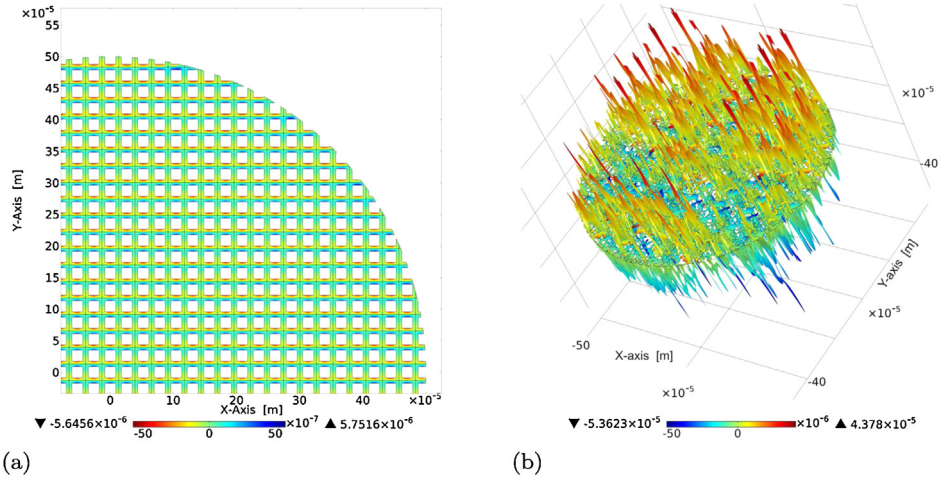

Fig. 5. (a) A partial view of the *x*-component for the vector field $\mathbf{b}_\gamma$ in a catalyst pellet built with RUC CC. (b) The *x*-component of the vector field $\mathbf{b}_\gamma$ in a catalyst pellet built with realistic porous media.

It is worth noticing that the difference between evaluated values of D_{eff} for the RUC CC used as reference and the values obtained with our realistic model of the porous microstructure is about 50.4 % for the *x* component and 66% for the *y* component. This implies strong variation. This result is in concordance with the literature [12,16] that suggests the complex microstructure of porous medium has a significant effect on the effective transport coefficients.

Regarding model 2:1 and model 4:1, it should be noted that the variation was less than 1%. Therefore, due to computational resources reasons only the model at scale 4:1 will be studied in more detail. Table 6 also shows the values predicted by the theoretical models previously reported [40–42]. It is important to highlight that the changes with respect to the reference model are in the order of 14% for the model of Maxwell [40], which considers the porous media as a dilute suspension of spheres; and 20% for the model of Wakao [42], whose expression is for a macropore system.

The estimated D_{eff} values allows to solve the mass pseudo-homogeneous transport model expressed by Eqs. (2)–(5) and the heterogeneous transport model expressed by Eqs. (8) and (9); and finally the effectiveness factor for non-isothermal case by means of Eq. (24). The Fig. 6a and b shows the concentration fields obtained with the COMSOL Multiphysics software, corresponding to the pseudo-homogeneous model and to the heterogeneous model, respectively.

Fig. 6c shows a comparison between concentration profiles obtained for a 1 mm diameter spherical catalyst pellet where a HDS reaction takes place, employing D_{eff} values obtained for

Table 6
D_{eff} values evaluated with RUC's, RUC's coupled, literature methods and our realistic porous media.

	Study	$\frac{\varepsilon_\gamma D_{xx}}{D_\gamma}$	$\frac{\varepsilon_\gamma D_{yy}}{D_\gamma}$	% relative error (respect to reference value)	
RUC	RUC CC	0.3602	0.3602	7.184	1.207
	RUC CA	0.336075	0.36462	9.985	9.7
	RUC RA	0.327516	0.328368		
	RUC CC				
	2×2	0.361 ± 0.005	0.361 ± 0.001	0.750	0.75
	4×4	0.361 ± 0.005	0.361 ± 0.001	1.023	1.023
	8×8	0.361 ± 0.005	0.361 ± 0.001	1.024	1.024
	16×16	0.361 ± 0.005	0.361 ± 0.001	1.551	1.551
RUC coupled	RUC CA				
	2×2	$0.338\pm1\times10^{-3}$	$0.365\pm4\times10^{-3}$	6.55	1.71
	4×4	$0.338\pm1\times10^{-3}$	$0.365\pm4\times10^{-3}$	5.59	2.38
	8×8	$0.338\pm1\times10^{-3}$	$0.365\pm4\times10^{-3}$	5.59	2.38
	16×16	$0.338\pm1\times10^{-3}$	$0.365\pm4\times10^{-3}$	5.59	2.38
	RUC RA	$0.33021\pm5\times10^{-6}$	$0.3300\pm1\times10^{-5}$		
	2×2	$0.338\pm1\times10^{-3}$	$0.365\pm4\times10^{-3}$	9.085	9.14
	4×4	$0.338\pm1\times10^{-3}$	$0.365\pm4\times10^{-3}$	9.071	9.117
	8×8	$0.338\pm1\times10^{-3}$	$0.365\pm4\times10^{-3}$	9.07	9.116
	16×16	$0.338\pm1\times10^{-3}$	$0.365\pm4\times10^{-3}$	9.07	9.116
	RUC CC	0.366211	0.366196	1.636	1.632
Pellet built with	RUC CA	0.340584	0.369287	5.765	2.456
	RUC RA	0.330906	0.331066	8.858	8.06
	Realistic Porous media	0.239539	0.21701	50.38	65.99
	Maxwell	0.445492	0.445492	19.141	19.141
Literature models	Weisberg	0.419709	0.419709	14.174	14.174
	Smith	0.298668	0.298668	20.68	20.68
	Model				

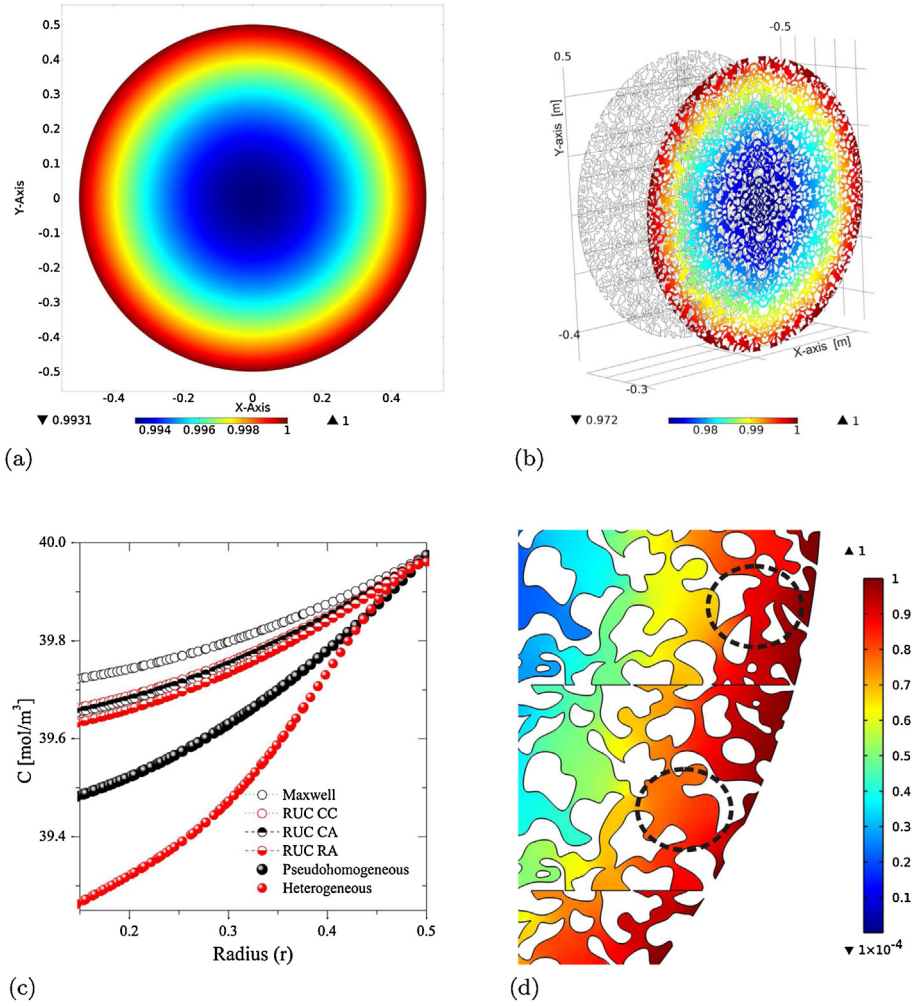

Fig. 6. (a) Dimensionless concentration field of a spherical catalyst from pseudo-homogeneous model, $\langle\Phi_{iso}\rangle$=0.3331. (b) Dimensionless concentration field of a spherical catalyst from heterogeneous model in 4:1 scale, $\langle\Phi_{iso}\rangle$=0.3331. (c) Dimensionless concentration field of a spherical catalyst from heterogeneous model at 4:1 scale, $\langle\Phi_{iso}\rangle$=0.3331 (d) Zoom in of dimensionless concentration field of a spherical catalyst from heterogeneous model at 4:1 scale, showing a zone (red circle) of more accessibility and a zone (black circle) of less accessibility, Φ_{iso} = 0.3331. (For interpretation of the references to color in this figure legend, the reader is referred to the web version of this article.)

diverse RUCs, also with models from literature presented in Table 6, and through our realistic model of the porous structure. It also presents the concentration profile corresponding to the heterogeneous model. As can be seen, the concentration profile using the value of D_{eff} corresponding to the RUC CC, is very different to that when D_{eff} from the model of the complex microstructure is employed. This result highlights the importance of the effect of the porous medium complex structure on the behavior of the catalytic pellet. Fig. 6d depicts a zoom in of the concentration field of the heterogeneous model solution, the asymmetry in concentration field is pointed out with two dashed circles, one shows an area with smaller accessibility and other shows an area with smaller easiness accessibility for the diffusive transport, the abovementioned is in agreement to that observed by other authors [3–5].

Fig. 7a shows a comparison of isothermal effectiveness factor evaluated from the pseudo- homogeneous model of mass transport, using the different values of D_{eff} calculated from the different RUC's, with the models from literature summarized in Table 6 and from the porous structure are. The effective diffusivity coefficient value for the porous structure was considered constant $D_{eff} = (D_{xx} + Dyy)/2$ in the transport model. In Fig. 7a, it is also shown the obtained effectiveness factor components of D_{eff}, considering the effective diffusion coefficient as a tensor.

Finally, the effectiveness factor obtained from the heterogeneous model of transport by diffusion with surface catalytic reaction is also shown by considering the porous microstructure.

It can be noticed that the effectiveness factor from the heterogeneous model is far from the factors obtained by simplified representations of the porous structure. Even more, although in less impact, the effectiveness factor with D_{eff} as a tensor, by considering the structure porous realistic, is significantly different from the heterogeneous mass transport model. Finally, Fig. 7b shows more clearly the difference between the values of the effectiveness factor from heterogeneous transport model and the values obtained from the pseudo-homogeneous models. In this figure two zones can be distinguished. The first one at $\phi < 0.4$ is where the difference between the factors for both models is greater, and the second at $\phi > 0.4$ is where the difference decreases. It is necessary to mention that the model with greater proximity to the heterogeneous model corresponds to the pseudo homogeneous with D_{eff} considered as a tensor and including the complexity of the porous structure.

Also, the fields for the vectors $\mathbf{b}_\sigma$ and $\mathbf{b}_\beta$ corresponding to the closure problem of transport of energy (Eqs. (21) and (22)) were evaluated. Fig. 8a shows the x-component of vector $\mathbf{b}_\beta$ in a RUC CA, whileFig. 8b shows the same result, only that for our realistic

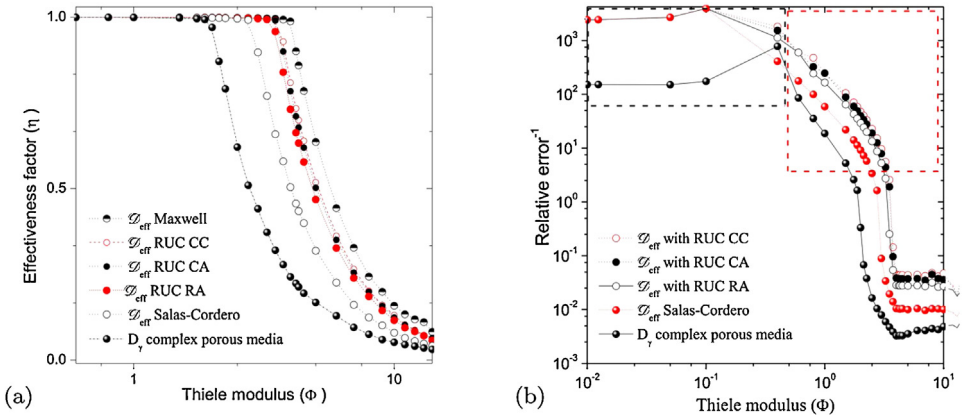

Fig. 7. (a) Comparison of isothermal effectiveness factors: pseudo-homogenous model vs. heterogeneous model obtained with D_{eff} values from different geometrical representations of porous structure. (b) Inverse of relative error between effectiveness factors obtained with D_{eff} values from different geometrical representations of porous structure.

model of the porous structure. The Keff values are obtained by Eq. (17) using the vector $\mathbf{b}_\beta$ fields from the two RUC's and our realistic model. It was found for the RUC CC, $K_{xx}/k_\beta = 2.4$ and $K_{yy}/k_\beta = 2.3$, while for the RUC CA $K_{xx}/k_\beta = 2.5$ and $K_{yy}/k_\beta = 3.07$; finally, the value from the realistic model is $K_{xx}/k_\beta = 7.2$ and $K_{yy}/k_\beta = 8.55$.

It is important to highlight that the boundary for the closure vectors for the heat transfer problem presents a rather difficult convergence. Table 7 shows values for the convergence of the RUC CC. It was not possible to establish a concrete value for the RUC RA and thus it was eliminated of this study. The simulations of the realistic model show a strong dependence on the number of mesh nodes. Around 1.3×10^6 mesh elements were required by the larger simulations that we were able to perform with the available computational resources.

From the effective conductivity values, it is possible to proceed to solve in a simultaneous way the mass and energy transport equations for the heterogeneous and pseudo-homogeneous model, using for the latter the obtained K_{eff} values in this work. Fig. 9a and b shows the temperature fields from the solution for the heterogeneous and pseudo- homogeneous model, respectively. In the comparison of the temperature and concentration fields it is observed that there are significant differences between the solutions of both models, for equivalent specifications in them reinforces the observation of the effect of the micro porous structure being from great importance. With the temperature and concentration fields for the catalytic pellet, we can proceed to obtain the non-isothermal effectiveness factors.

Fig. 10a shows a comparison of the temperature and concentration fields for the non-isothermal case. These were obtained from the pseudo-homogeneous model, where the effective coefficients came from the RUCS and from the proposed model of the porous structure. Fig. 10b also depicts the fields obtained from the heterogeneous model. The series referred as Maxwell, correspond to the fields of temperature and concentration obtained with the pseudohomogeneous model, using the diffusivity and conductivity effective coefficients obtained with the theoretical pattern of Maxwell [40]. The RUC CC and RUC CA series correspond to the fields of temperature and concentration coming from the pseudohomogeneous pattern, using the diffusivity and conductivity effective coefficients coming from the solution of the field of the closure vector in the centered square unitary cells (Figs. 3a and 8a) and square alternate unitary cell (Fig. 3b). The fields of temperature and concentration coming from the heterogeneous pattern are also shown. These were produced by using the diffusivity and conductivity effective coefficients coming from the solution of the field of the closure vector in the realistic model (Figs. 5a and 8b). The parameters used in the evaluation of the temperature and concentration fields were determined using the properties and kinetic parameters shown in Tables 1 and 3 and according to the definitions in Table 5. Fig. 10b shows that the complexity of the geometry is not captured in an appropriate way by representations as simple as the RUC's. Fig. 10b shows a comparison of the non-isothermal effectiveness factors from pseudo-homogeneous and pseudo-homogeneous models and can be appreciated how

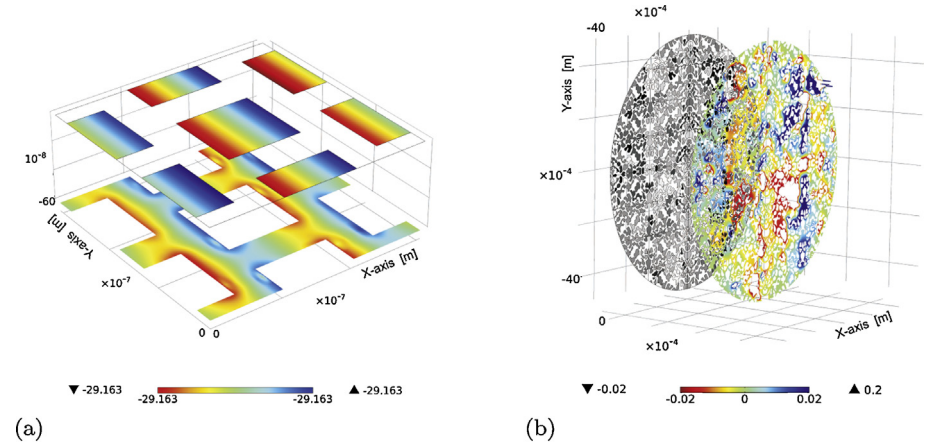

Fig. 8. (a) Vector $\mathbf{b}_\beta$, x-component field in a RUC CC. (b) Vector $\mathbf{b}_\beta$, x-component field in a realistic porous structure.

Table 7
Statistics of the K_{eff} convergence in a RUC CC.

Mesh element number	Iteration number	Simulation time (h)	% Relative error (K_{xx})	% Relative error (K_{yy})
568	–	1.9	11.99	5.22
1160	2.042	1.7	7.78	10.06
2428	2.093	3.8	3.45	8.72
5230	2.15	8.2	1.18	2.19
10589	2.046	16.7	0.98	0.81

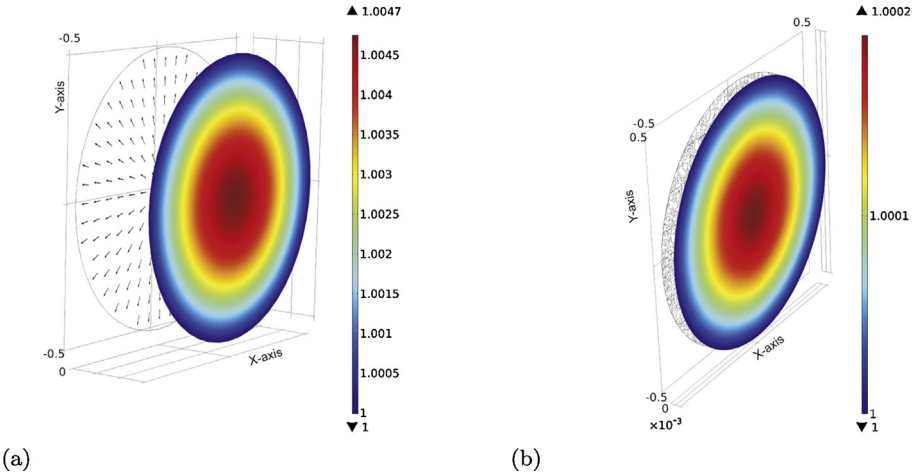

Fig. 9. (a) Dimensionless Temperature field of a spherical catalyst from heterogeneous model, $\langle\Phi_{iso}\rangle$=0.3331 and β=0.7. (b) Dimensionless Temperature field of a spherical catalyst from pseudo-homogeneous model, $\langle\Phi_{iso}\rangle$=0.3331 and β=0.7.

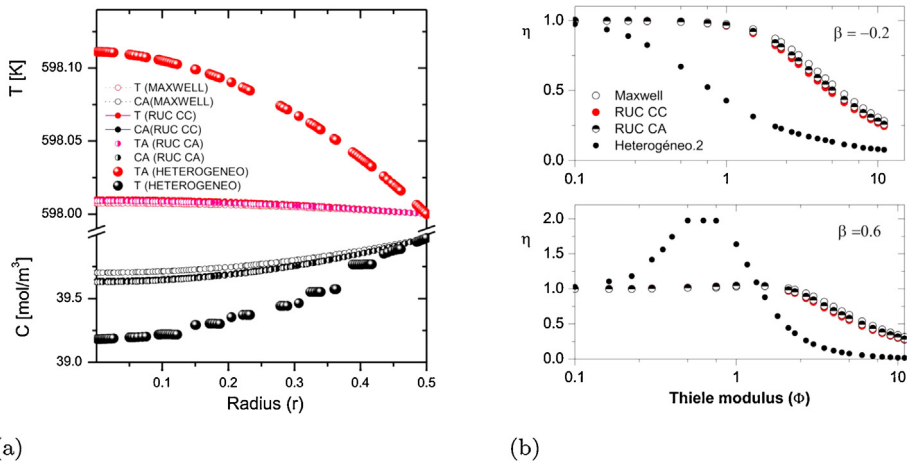

Fig. 10. (a) Temperature and concentration fields from non isothermal mass and energy transport model $\langle\Phi_{iso}\rangle$=0.3331. (b) No isothermal effectiveness factor comparison for pseudo-homogeneous and heterogeneous models $\langle\Phi_{iso}\rangle$=0.3331.

they differ one from another and this is evidence of the microstructure influence over non-isothermal effectiveness factors. It is worth pointing out that these differences become more significant when Thiele modulus increases (i.e. by increasing particle diameter). Despite the incorporation of further characteristics of the porous structure like complex geometry and anisotropy, it should not be left out that this study is based on 2D modeling and this still may imply certain degree of inaccuracy. It is worth mentioning, however, that in the context of averaging volume methodology the differences between effective transport coefficients values calculated from 2D and 3D models are expected to not be significant [37].

4. Conclusions

A realistic geometric model of the porous microstructure for a spherical catalyst pellet was developed. In such a porous medium the mass and energy effective coefficients of transport were calculated and the effect of the structure complexity on these c coefficients was evaluated. It can be concluded that these transport coefficients can be up to 65% different depending on whether a simple or complex porous structure is used. In addition, the concentration and temperature fields were evaluated using a pseudo-homogeneous model and a heterogeneous one. Furthermore, the isothermal and non-isothermal effectiveness factors for a HDS

process were evaluated and it was concluded that the microstructure has important impact on their values. These were higher when obtained through pseudo-homogeneous models. The use of non-isothermal effectiveness factors leads to multiplicity of stationary states that are expected for exothermic reactions. Finally, a rather simplistic geometric model of the porous structure does not show adequacy to represent the mass and energy transport in catalytic pellet and thus a more realistic geometric model of the porous structure is required.

Acknowledgements

To Eymi Vargas, Alicia Vicenttín, Aurora Catalan and Enrique Blanco for writing assistance.

References

[1] R.B. Bird, W.E. Stewart, E.N. Lighfoot, Transport phenomena, Wiley, New York, 1960.
[2] R. Aris, The Mathematical Theory of Diffusion and Reaction in Permeable Catalysts, Clarendon Press, Oxford, 1975.
[3] B.J. Sapoval, S. Andrade, M. Filoche, Chemical Engineering Science 56 (2001) 5011–5023.
[4] M. Adler Pierre, Porous Media: Geometry and Transports, Butterworth-Heinemann, Boston, 1992.
[5] M. Sahimi, J. Appl. Math. Mech. 76 (1996) 230.
[6] H. Davarzani, M. Marcoux, M. Quintard, Int. J. Heat Mass Transfer 53 (2010) 1514–1528.
[7] Jin-Hwan Kim, J. Alberto Ochoa, Stephen Whitaker, Diffusion in anisotropic porous media, Transport Porous Media 2 (1987) 327–356.
[8] J.A. Ochoa-Tapia, P. Stroeve, S. Whitaker, Chem. Eng. Sci. 41 (1986) 2999–3013.
[9] I. Nozad, R.G. Carbonell, S. Whitaker, Chem. Eng. Sci. 40 (1985) 843–855.
[10] S. Whitaker, Flow in porous media i: A theoretical derivation of darcy's law, Transport Porous Media 1 (1986) 3–25.
[11] D. Buyuktas, W. Wallender, Heat Mass Transfer 40 (2004) 261–270.
[12] A.M. Sales-Cruz, O.A. Luévano Rivas, J.A. Ochoa-Tapia, XXXII Encuentro Nacional y 1er Congreso Internacional de Ingeniería Química, 2011, p. 2136.
[13] L. Zhang, N.A. Seaton, Chem. Eng. Sci. 47 (1994) 41–50.
[14] M.O. Coppens, G.F. Froment, Eng. Sci. 50 (1995) 1013–1026.
[15] T.E. Koha, S. Moshe, D. Avnir, Eng. Sci. 46 (1991) 2787–2798.
[16] Z.S. Lui, D. Mu, C. Huang, N. Djilali, Microfluidics Nanofluids 4 (2008) 257–260.
[17] S. Whitaker, The Method of Volume Averaging, Kluwer Academic Publishers, Netherlands, 1999.
[18] F.J. Valdés-Parada, B. Goyeau, J.A. Ochoa-Tapia, Transport Porous Media 78 (2009) 459–476.
[19] M. Ehrhardt, Coupled Fluid Flow in Energy, Biology and Environmental Research, volume 1, Bentham Science Publishers, Germany, 2012.
[20] J.B. Rawlings, J.G. Ekerdt, Chemical Reactor Analysis and Desing Fundamentals, vol. 2, Nob Hill Publishing, Winsconsin, 2002.
[21] K.G. Mittal, J.R. Rai, K.M. Murad, Indian Chem. Eng. 9 (1977) 18–23.
[22] J. Lee, D.H. Kim, Chem. Eng. Sci. 62 (2007) 2179–2186.
[23] Y.P. Sun, S.B. Lui, S. Keith, Chem. Eng. J. 102 (2004) 1–10.
[24] J. Hong, W.C. Hecker, T.H. Fletcher, Proceedings of the Combustion Institute, 2000, pp. 2215–2223.
[25] S. Shokri, S. Zarrinpashne, Petroleum Coal 48 (2006) 27–33.
[26] M.J. Macias, R.D. Morales, A. Ramirez-López, Int. J. Chem. Reactor Eng. 7 (2009) 21.
[27] R. Gutfraind, M. Sheintuch, Chem. Eng. Sci. 47 (1992) 4425–4433.
[28] S.R. Karur, P.A. Ramachandran, AIChe J. 42 (2004) 383–390.
[29] C. Botchwey, Syntheses, Characterization and Kinetics of Nickel-Tungsten Nitride Catalysts for Hydrotreating of Gas Oil, Department of Chemical Engineering, University of Saskatchewan, Saskatoon, 2010 (Ph.D. Dissertation).
[30] G.F. Froment, K.B. Bischoff, Chemical Reactor Analysis and Desing, John Wiley & Sons, New York, 1979.
[31] M. Auset, A.A. Keller, Water Resour. Res. 40 (2004) 13.
[32] M.S. Rana, J. Ancheyta, P. Rayo, S.K. Maity, Rev. Mexicana Ing. Quí m. 5 (2006) 227–235.
[33] K. Muramatsu, B. Gómez, A. Zárate, L.M. Juárez, J.F. Rodríquez, J.J. Menéndez, Tecnol. Cien. Educ. 1 (1989) 49–55.
[34] V.V. Ranade, R.V. Chaudhari, P.R. Gunjal, Trickle Bed Reactors, Elsevier, Spain, 2011.
[35] W.G. Gray, Chem. Eng. Sci. 30 (1975) 229–233.
[36] A. Bensoussan, J.L. Lions, G. Papanicolaou, Asymptotic Analysis for Periodic Media, North-Holland Publishing Company, Amsterdam, 1978.
[37] J.A. Ochoa-Tapia, P. Stroeve, S. Whitaker, Chem. Eng. Sci. 49 (1994).
[38] E.A. Saez, J.C. Perfetti, I. Rusinek, Transport Porous Media 6 (1991) 143–158.
[39] M. Quintard, S. Whitaker, Transport Porous Media 14 (1993) 163–177.
[40] J.C. Maxwell, Treatise on Electricity and Magnetism, Clarendon Press, Oxford, 1954.
[41] L. Weissber, J. Appl. Phys. 34, 2636–2639.
[42] N. Wakao, J.M. Smith, Chem. Eng. Sci. 17 (1962) 347–825.